

Swept-Angle Synthetic Wavelength Interferometry: Supplementary Material

Alankar Kotwal¹, Anat Levin², and Ioannis Gkioulekas¹

¹Carnegie Mellon University, ²Technion

1. Proof of Equation (2) of the main paper

Synthetic wavelength interferometry uses illumination comprising two distinct, but narrowly-separated, lasers that are incoherent with each other. We denote the wavelengths of these lasers λ and $\lambda/_{1+\epsilon}$, corresponding to wavenumbers $\kappa \equiv 2\pi/\lambda$ and $(1 + \epsilon)\kappa$, respectively. In full-field SWI, the outputs of these lasers are collimated by a lens into a beam covering the field of view. The laser with wavelength λ results in a wavefront parallel to the optical axis. The corresponding field propagating towards the beamsplitter is

$$\mathbf{u}_i^\kappa(x, z) = \exp(-i\kappa z). \quad (1)$$

When the scene point at x is placed at a distance $d(x)$ from the beamsplitter, the illumination travels $2d(x)$ in the scene arm, accounting for the propagation to the scene and back. Then, the field due to the scene at the sensor pixel x is

$$\mathbf{u}_s^\kappa(x) = \exp(-i\kappa(2d(x) + l_0)), \quad (2)$$

where l_0 is the travel distance from the lens to the beamsplitter and the beamsplitter to the sensor. Similarly, when the reference arm is at a distance l from the beamsplitter, the field due to the reference arm at sensor pixel x is

$$\mathbf{u}_r^\kappa(x, l) = \exp(-i\kappa(2l + l_0)). \quad (3)$$

Then, the correlation $\mathcal{C}^\kappa(x, l)$ for the wavelength λ equals

$$\mathcal{C}^\kappa(x, l) = \mathbf{u}_s(x)\mathbf{u}_r^*(x, l) \quad (4)$$

$$= \exp(-2i\kappa(d(x) + l_0)) \exp(i\kappa(l + l_0)) \quad (5)$$

$$= \exp(-2i\kappa(d(x) - l)). \quad (6)$$

As the two lasers are incoherent with each other, there are no cross-correlations between the fields. Thus, $\mathcal{C}(x, l)$ for both lasers equals the *incoherent* sum of their correlations:

$$\mathcal{C}(x, l) = \mathcal{C}^\kappa(x, l) + \mathcal{C}^{(1+\epsilon)\kappa}(x, l) \quad (7)$$

$$= \exp(-2i\kappa(d(x) - l)) + \exp(-2i\kappa(1 + \epsilon)(d(x) - l)) \quad (8)$$

$$= \exp(-2i\kappa(d(x) - l)) [1 + \exp(-2i\kappa\epsilon(d(x) - l))]. \quad (9)$$

thus proving Equation (2) from the main paper.

2. Scanning versus full-field comparison

Scan points for equal-time acquisition. In Figure 9 of the main paper, we show depth reconstructions with full-field swept-angle SWI and upsampled point scanning SWI

for the $\{4, 4\}$ -shift algorithm. To emulate point scanning, we downsampled the SWI depth by a factor of 35 in each dimension, and claimed that this corresponds to an equal-time comparison for a 30 kHz MEMS scanner. Here, we detail this calculation.

Our swept-angle SWI system, for scenes with very low reflectivity, operates at 1 Hz. In the equivalent time of 1 s, the scanner must perform 16 passes over the scene to take the 16 measurements required for the $\{4, 4\}$ -shift algorithm. This makes the maximum number of points the scanner can measure in two dimensions $30000/16 = 1875$. In one dimension, this translates to $\sqrt{1875} \approx 43$ points. Our images have approximate dimension 1600×1300 . Distributing these points equally along the larger dimension yields a downsampling factor of $1600/43 \approx 35$.

We note that this calculation is already favorable for the scanning system, for two reasons. First, the typical scan rate will be lower than the nominal scan rate of 30 kHz, because of the need to scan a larger field of view, or the inability to drive both axes at resonant mode. Second, for scenes with high reflectivity (e.g., metallic scenes), our setup operates at 10 Hz, and thus the number of scanned points for the scanning system should be $10\times$ fewer.

Challenges for achieving micrometer lateral resolutions with scanning systems. The main paper discusses some of the challenges associated with achieving micrometer lateral resolution using a scanning system operating in *resonant mode* (e.g., using Lissajous scanning). Here, we discuss in more detail additional challenges in achieving micrometer lateral resolutions using a scanning system. Doing so requires: (i) a laser beam that can be collimated or focused at a few micrometers; (ii) a MEMS mirror capable of scanning at high-enough angular resolution to translate the laser beam a few microns on the scene surface; and (iii) acquisition time long enough to scan a megapixel-size grid on the scene. Each of these requirements is difficult to achieve:

- (i) The diameter of a Gaussian laser beam is inversely proportional to its divergence [5, Chapter 4]. The smaller the beam diameter, the larger the divergence. At 780 nm, a laser beam with a diameter of $1 \mu\text{m}$ grows in diameter by 10% every 2 m. Therefore, maintaining collimation diameter of $1 \mu\text{m}$ is challenging except for very small working distances.

As an alternative to using a thin, collimated laser beams, we can use a beam that is focused at each point on the scene. Contrary to micron-scale beam waists, it is possible to focus single-model lasers to pixel-size spot sizes [5, Chapter 9] However, focusing the laser beam onto the scanned scene points sharply decreases the depth of field of the imaging system: Whereas, in the case of a collimated beam, the depth of field is limited by the divergence of the collimated beam, in the case of a focused beam, it is limited by the quadratic phase profile of the focused spot. Effectively, to use this focused setup, we need another axial scan to ensure that the scanned post is within the depth of field, which only adds to acquisition time.

- (ii) Top-of-the-line scanning micromirrors typically have angular scanning resolutions of $10 \mu\text{rad}$ [4]. The maximum working distance such that this would correspond to micrometer lateral resolution is 10 cm.
- (iii) The scanning micromirror needs to be run in “point-to-point scanning mode” [4], where the micromirror stops at every desired position. The best settling times for step mirror deflections are around $100 \mu\text{s}$ [4]. Using these numbers, for a megapixel image, the micromirror rotations require acquisition time around 100 s.

A swept-angle full-field interferometer does not need to perform lateral scanning of the image plane. Instead, it accomplishes direct-only (i.e., coaxial) imaging by scanning an area in the focal plane of the collimating lens, an operation that can be done in the resonant mode of a MEMS mirror within exposure and at low lateral resolution.

3. Additional experiments

Trade-off between acquisition time and depth quality. The theoretical minimum number of measurements needed to reconstruct depth using SWI is 9 ($M = N = 3$). However, increasing M and N makes the depth reconstruction robust to measurement and speckle noise, yielding higher quality depth. There is, therefore, a trade-off between number of measurements $M \cdot N$ and depth quality.

Besides number of measurements, another factor contributing to acquisition time is the MEMS mirror scan we perform to create swept-angle illumination. If we decrease acquisition time, giving the mirror less time to complete one full scan of the focal plane of the collimating lens, the spatial density of scanned points on focal plane decreases. This reduces the effectiveness of rejecting indirect light, and therefore reduces depth quality. This, again, creates a trade-off between acquisition time and depth quality.

In Figure 1, we demonstrate the effect of both these factors on depth quality. On the horizontal dimension, we use different $\{M, N\}$ -shift phase retrieval algorithms, and on

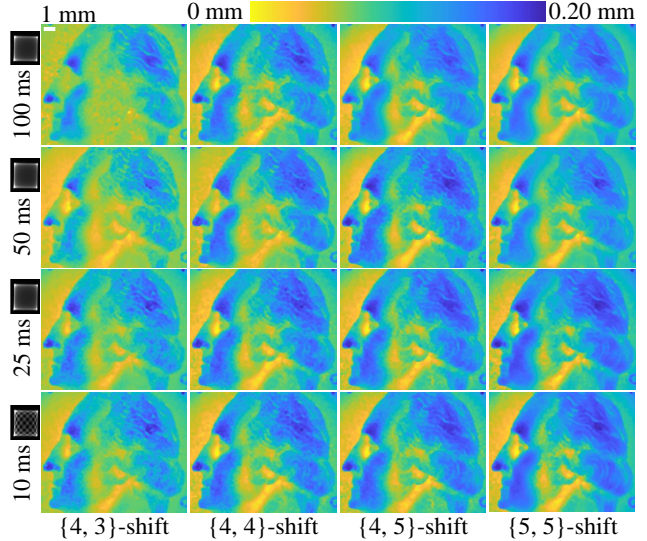


Figure 1. **Depth quality and acquisition time.** We show qualitatively the effects of per-image acquisition time (dictated by the period of the MEMS mirror scan) and the number of images acquired $M \cdot N$ on the quality of the reconstructed depth. The pattern in the black box next to per-image times is the scanned emission area in the focal plane of the illumination lens.

the vertical dimension, we use different per-image acquisition times, corresponding to different focal plane scanning resolutions. Using higher M and N allows us to reduce the per-image acquisition time, by requiring a lower scanning density for equal depth quality. In particular, the 100 ms scan with the $\{4, 5\}$ -shift algorithm performs as well as the 10 ms scan with the $\{5, 5\}$ -shift algorithm, allowing us to reduce total acquisition time from 2 s to 250 ms.

Tunable depth range. The use of two wavelengths in synthetic wavelength interferometry makes it possible to control the unambiguous depth range: By decreasing the separation $\kappa\epsilon$ between the two laser wavelengths, we increase the unambiguous depth range, at the cost of decreasing depth resolution. In particular, picometer separations in wavelengths result in synthetic wavelengths of centimeters. We use this to scan the *macroscopic* scenes in Figure 2, which have a depth range of approximately 1 cm. In all three scenes, the use of swept-angle illumination greatly improves reconstruction quality, by mitigating the effects of the significant subsurface scattering present in all scenes.

We note that achieving picometer-scale wavelength separation requires using current-based tuning of the wavelength of the DBR lasers in our setup. The DBR lasers have a linear response of wavelength to current near their operating point, and tuning current by 50 mA gives picometer-scale wavelength separations.

Robustness to ambient light. In Figure 3, we demonstrate the robustness of our method to ambient light on the toy cup scene from Figure 2. We shine a spotlight on the scene such that the signal-to-background ratio (SBR) of the laser

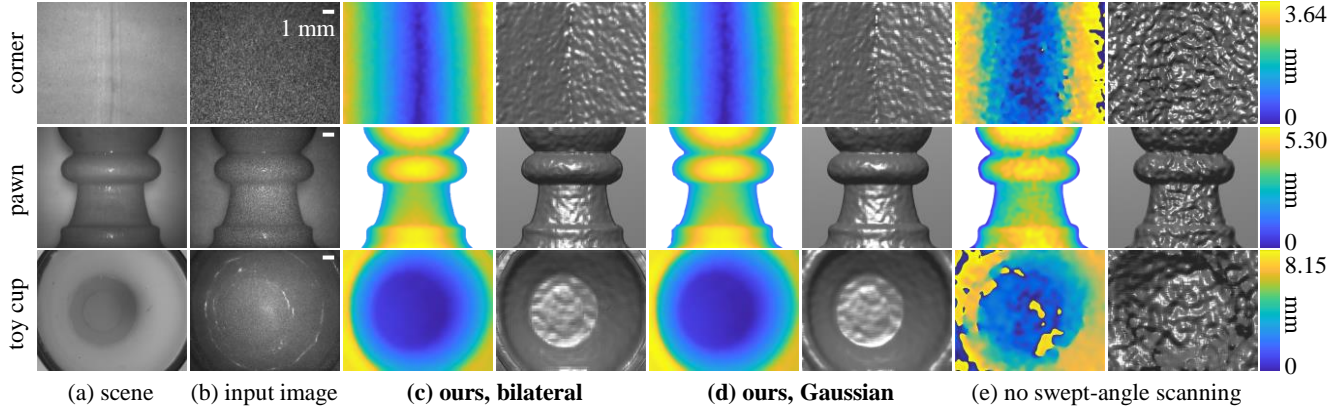


Figure 2. **Depth reconstruction.** Depth maps (left) and surface renderings (right) acquired using full-field SWI with: (c) swept-angle scanning and bilateral filtering; (d) swept-angle scanning and Gaussian filtering; (e) no swept-angle scanning and with Gaussian filtering.

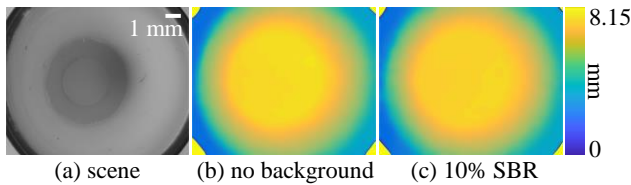


Figure 3. **Robustness to ambient light.** In (c), we shine external light on the sample so that the signal-to-background ratio (SBR) our laser illumination to ambient noise is 0.1. This greatly decreases the contrast of the interference speckle pattern. Despite this, there is little degradation in the quality of our recovered depth.

illumination to ambient light is 0.1. Ambient light adds to the intensity measurement at the camera, but not to interference, thus reducing interference contrast and potentially degrading the depth reconstruction. However, we see that at this SBR, the depth recovered from the toy cup scene (Figure 3(d)) is very close to the depth recovered without ambient light (Figure 3(c)). In addition, we can further reject ambient light by using an ultra-narrow spectral filter centered at the average illumination wavelength. This is possible because SWI uses illumination comprising two very narrowly-separated wavelengths.

Depth accuracy. We show here the data we captured to assess our depth accuracy in Table 1 of the main paper. Figure 4 plots, on top, the estimated SWI depth relative to the ground truth depth provided by the scene translation stage. Figure 4(a) is captured with the swept-angle mechanism, whereas Figure 4(b) is captured with the mechanism off. Comparing the two figures, we see that the measured depth correlates with the ground truth depth a lot stronger when we use swept-angle illumination versus when we do not.

Figure 4(c) and Figure 4(d) respectively show the same experiment performed at a *macroscopic* synthetic wavelength of 16 mm, the same as in Figure 2. These measurements also depict that swept-angle scanning is critical for micron-scale depth sensing. We show the error numbers from this experiment, similar to Table 1 in the main paper,

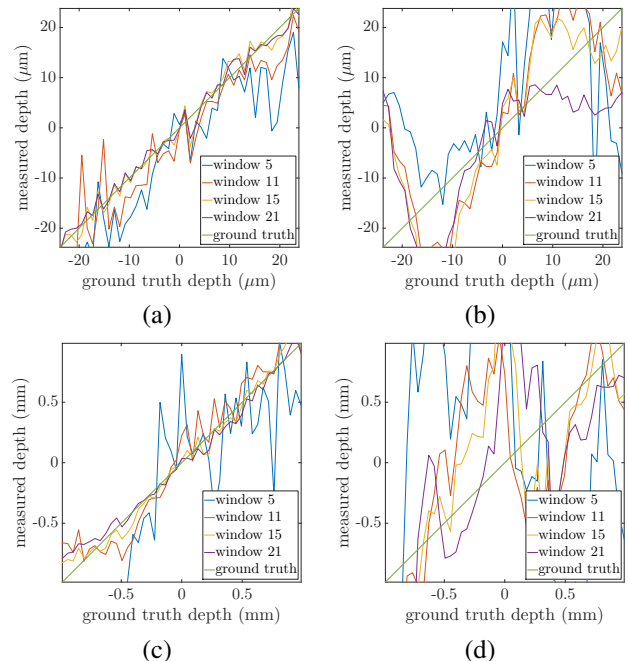


Figure 4. **Testing the depth resolution of our method.** We place the chocolate scene from Figure 5 at different distances from the camera using a translation stage and capture measurements using our method at each position. We do this under four conditions: (a) microscopic synthetic wavelength with swept-angle, (b) microscopic synthetic wavelength without swept-angle, (c) macroscopic synthetic wavelength with swept-angle, and (d) macroscopic synthetic wavelength without swept-angle. In each case, we plot the depth measured by our method against the ground truth position of the scene provided by the translation stage. The window parameter in the plots is the size of the Gaussian blur kernel.

in Table 1. With a kernel width of 150 μm , we are able to achieve depth accuracies of 50 μm .

Comparison with full-field OCT. As mentioned in the main paper, depth sensing with full-field spatially-incoherent OCT achieves unambiguous depth ranges up to centimeters at micrometer axial resolutions. Here, we

Table 1. **Depth accuracy with synthetic wavelength** 16 mm. MedAE is the median absolute error between ground truth and estimated depth. Kernel width is the lateral size of the speckle blur filter. All quantities are in μm .

kernel width	with swept-angle		w/o swept-angle	
	RMSE	MedAE	RMSE	MedAE
7	471.4	300.3	1267.2	1351.0
15	167.1	120.5	577.9	501.9
21	78.7	50.9	609.5	412.2
30	81.7	49.6	605.7	334.4

demonstrate that swept-angle SWI approximates the reconstruction quality of full-field OCT, while being $50\times$ faster. Figures 5 and 6 compare the performance of swept-angle SWI with full-field OCT implemented as in Gkioulekas et al. [1]. We also depict differences between swept-angle SWI and OCT depth reconstructions.

We use time-domain OCT to capture these scenes. Time-domain OCT requires a reference mirror scan spanning the depth range of the scene spaced at equal intervals of the desired depth resolution. For $500\ \mu\text{m}$ depth range and $1\ \mu\text{m}$ axial resolution, the number of measurements OCT requires that is 500. By contrast, SWI can capture depth with comparable quality in $M \cdot N$ measurements. For the comparison in Figure 5, we use $4 \cdot 4 = 16$ measurements, which makes SWI $30\times$ faster than OCT at comparable reconstruction quality. As we show in Figure 1, we can achieve similar reconstruction quality using SWI with $3 \cdot 3 = 9$ measurements, making SWI $50\times$ faster than OCT.

4. Acquisition setup

We discuss here the engineering details of the setup implementing swept-angle synthetic wavelength interferometry. The schematic and a picture of the setup are shown in Figure 5(c) of the main paper. We use similar components as in the setup of Kotwal et al. [2], and replicate the implementation details below for completeness.

Light source. We use near-infrared single frequency tunable laser diodes from Thorlabs (DBR780PN, 780 nm, 45 mW, 1 MHz linewidth). These laser diodes are tunable in wavelength by adjusting either operating current or temperature of the diode. To create small wavelength separations (of the order of 0.01 nm), we modulate the operating current of one laser diode with a square waveform, thus create two time-multiplexed wavelengths. To create larger separations (of the order of 1 nm), we use two different laser diodes selected at the appropriate central wavelengths. This is possible because the central wavelengths of separately manufactured laser diodes vary in a $\pm 2\ \text{nm}$ region around 780 nm. We found that for accurate depth recovery, it is important for the light sources to be monochromatic (single longitudinal mode), stable in wavelength and power, and accurately tunable. We experimented with multiple alter-

natives and encountered problems with either stability, tunability or monochromaticity. We found the DBR lasers from Thorlabs optimal in all these aspects.

Calibrating the synthetic wavelength. The synthetic wavelength resulting from this illumination is very sensitive to the separation between the two wavelengths, especially at microscopic scales. Therefore, after selecting a pair of lasers or current levels for an approximate synthetic wavelength, it is necessary to estimate the actual synthetic wavelength accurately. To do this, we measure the envelope sinusoid for a planar diffuser scene at a dense collection of reference arm positions. We then fit a sinusoid to these measurements to estimate the synthetic wavelength.

Mechanism for swept-angle scanning. We use two fast-rotating mirrors to scan the laser beam in $1^\circ \times 1^\circ$ angular pattern at slightly separated kHz frequencies, as shown by Kotwal et al. [2] and Liu et al. [3]. A 35 mm Nikon prime lens then maps beam orientation to spatial coordinates at the focal plane of the illumination lens, creating the effective area light source for swept-angle illumination. The emission area for this effective light source is a dense Lissajous curve that approximates a square. Figure 7 shows an example scanning pattern.

In practice, we use much denser scanning patterns, but show the coarse one in the inset only to make the Lissajous pattern visible. We note that our actual scanning patterns are still at much lower resolution than the pixel-level resolution that would be required in a scanning SWI system that raster scans the image plane. For this choice of scanning resolution, we follow Gkioulekas et al. [1] and Kotwal et al. [2], who show that the extent of the scanning pattern is more important than scanning density. Intuitively, as we decrease scanning density, we improve SNR (more light paths contribute to interference component, speckle contrast is stronger), at the cost of rejecting less indirect illumination. Figure 1 shows the scanning patterns we use for experiments (insets), and experimentally quantifies this trade-off.

Illumination lens. We place the above light source in the focal plane of a 200 mm Nikon prime lens to generate the swept-angle illumination. Photographic lenses perform superior to AR-coated achromatic doublets in terms of spherical and chromatic aberration, therefore resulting in significantly lesser distortion in the generated wavefront.

Interreflections. Interreflections are problematic for us because our illumination is temporally coherent. Interreflections introduce multiple light paths that interfere with each



Figure 7. Lissajous curve scanned in the focal plane of the collimating lens.

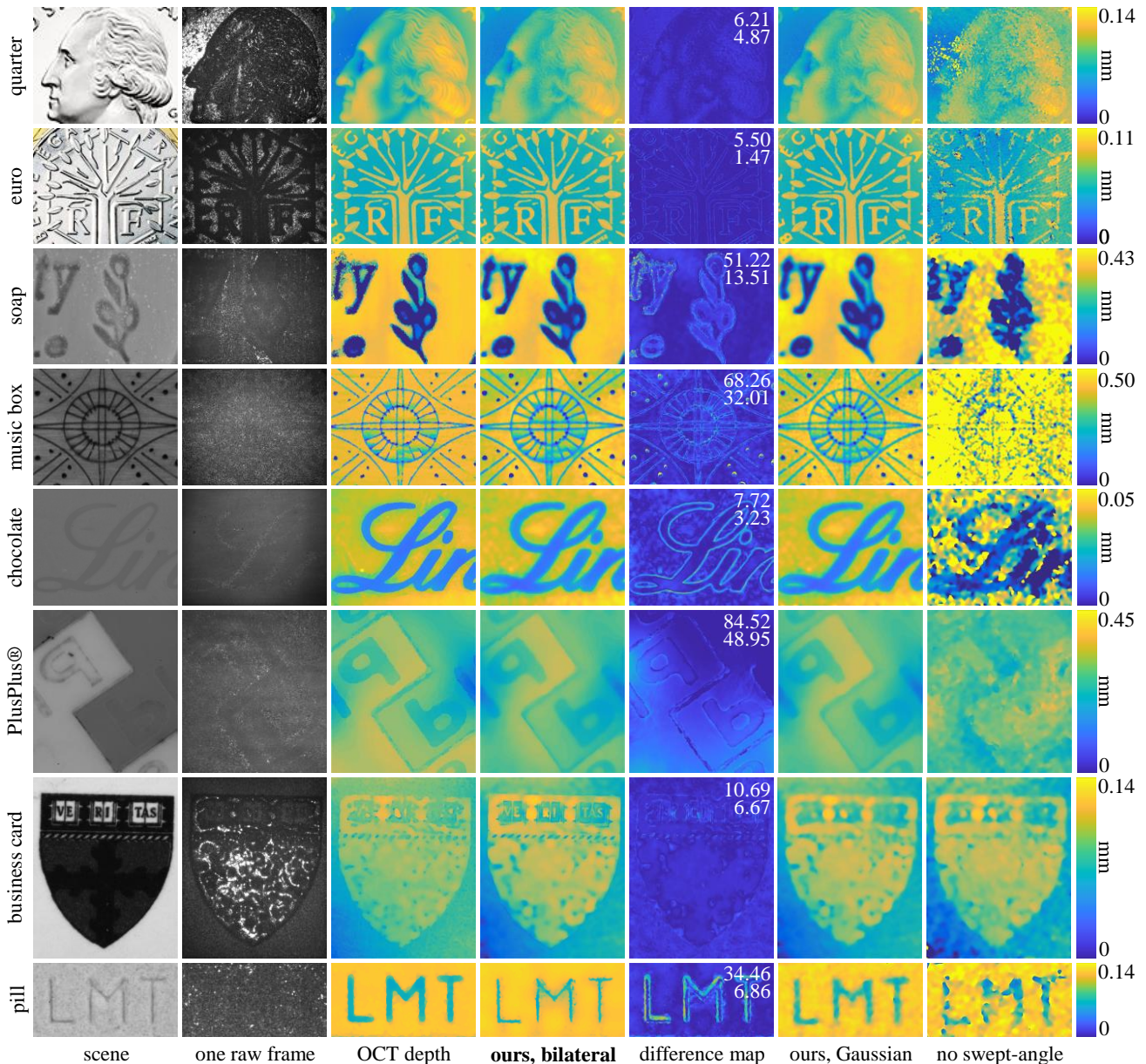


Figure 5. **Comparing swept-angle SWI and full-field OCT in microscopic scenes.** The difference maps show the absolute difference between recovered OCT and swept-angle SWI depths, and report the root-mean-square (top) and mean absolute (bottom) differences between the two. The OCT depths are captured at a resolution comparable to swept-angle SWI.

other to create strong spurious fringes. Such fringes suppress the contrast of our speckle signal. The optics we use are coated with anti-reflective films designed for our laser wavelengths to reduce interreflections. We also deliberately misalign our optics with sub-degree rotations from the ideal alignment to avoid strong interreflections.

Beamsplitter. We use a 50:50 plate beamsplitter, as pellicle and cube beamsplitters create strong fringes. As above, we misalign the beamsplitter to avoid interreflections.

Mirrors. We use high-quality mirrors of guaranteed $\lambda/4$

flatness to ensure a uniform phase reference throughout the field of view of the camera.

Translation stage. We use a high-precision motorized linear translation stage with a positioning accuracy of up to 10 nm and minimum incremental motion of 1 nm. For high-resolution depth recovery, it is important that the mirror positions images are captured at accurate sub-wavelength scales. In addition, it is important that the translation stage guarantee low-positioning-noise operation.

Camera lens. Our scenes are sized at the order of 1 inch.

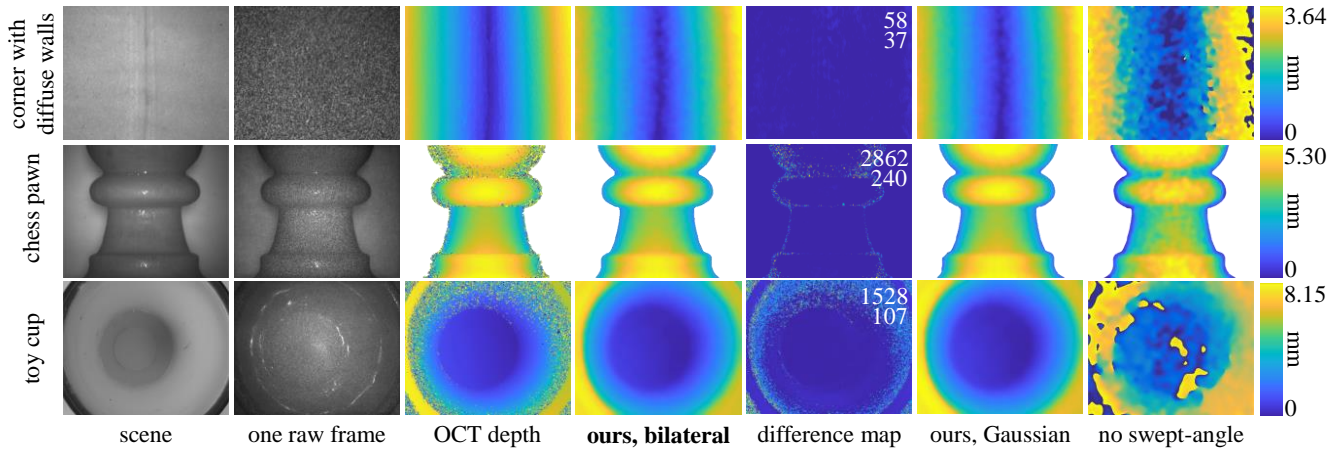


Figure 6. **Comparing swept-angle SWI and full-field OCT in macroscopic scenes.** The difference maps show the absolute difference between recovered OCT and swept-angle SWI depths, and report the root-mean-square (top) and mean absolute (bottom) differences between the two. The OCT depths are captured at a resolution comparable to swept-angle SWI.

Table 2. List of major components used in the optical setup of Figure 5(c) of the main paper.

description	quantity	model name	company
single-frequency lasers, 780 nm CWL, 45 mW power	2	DBR780PN	Thorlabs
benchtop laser diode current controller, ± 500 mA HV	2	LDC205C	Thorlabs
benchtop temperature controller, ± 2 A / 12 WW	2	TED200C	Thorlabs
1 \times 2 polarization-maintaining fiber coupler, 780 \pm 15 nm	1	PN780R5A1	Thorlabs
reflective FC/APC fiber collimator	1	RC04APC-P01	Thorlabs
2 \times beam expander	1	GBE02-B	Thorlabs
2-axis galvanometer mirror set	1	GVS202	Thorlabs
function generator	2	SDG1025	Siglent
35 mm compound lens	1	AF Micro Nikkor 35mm 1:4 D IF-ED	Nikon
200 mm compound lens	1	AF Micro Nikkor 200mm 1:4 D IF-ED	Nikon
25 mm \times 36 mm plate beamsplitter	3	BSW10R	Thorlabs
1 inch round protected Aluminum mirror	3	ME1-G01	Thorlabs
2 inch absorptive neutral density filter kit	1	NEK01S	Thorlabs
ultra-precision linear motor stage, 16 cm travel	1	XMS160	Newport Corporation
ethernet driver for linear stage	1	XPS-Q2	Newport Corporation
780.5 \pm 1 nm OD6 ultra-narrow spectral filter	1	-	Alluxa
180 mm compound lens	1	EF 180mm f/3.5L Macro USM	Canon
8 MP CCD color camera with Birger EF mount	1	PRO-GT3400-09	Allied Vision Technologies

Therefore, we benefit from a lens that achieves high magnifications (1:1 reproduction ratio). This also provides better contrast due to less speckle averaging (interference signal is blurred with the pixel box when captured with the camera). We use a 180 mm Canon prime macro lens for the camera. **Camera.** We use a machine vision camera from Allied Vision with a high-sensitivity CCD sensor of 8 MP resolution, and pixel size 3.5 μ m. A sensor with a small pixel pitch averages interference speckle over a smaller spatial area, therefore allowing us to resolve finer lateral detail. We use a camera with the sensor protective glass removed. This is critical to avoid spurious fringes from interreflections.

Neutral density filters. We use absorptive neutral density filters to optimize interference contrast by making the intensities of both interferometer arms equal.

Alignment. For depth estimation accurate to micron-scales,

the optical setup requires very careful alignment. To avoid as much human error as possible, we build the illumination side and the beamsplitter holder on a rigid cage system constructed with components from Thorlabs. To ensure a mean direction of light propagation that's parallel to the optical axis of the interferometer, we tune the steering mirrors electronically by adjusting their driving waveform's DC offset. We then align the reference mirror and camera using the alignment technique described by Gkioulekas et al. [1].

Component list. For reproducibility, Table 2 gives a list of the important components used in our implementation.

5. Code and algorithms

We provide in Figure 8 an implementation of the {4, 4}-shift phase retrieval algorithm for recovering depth from measurements made with four subwavelength shifts and the

four-bucket algorithm. The code assumes that the measurements are stored in a variable `frames` of size $H \times W \times 4 \times 4$, where H and W are the height and width of the measured images respectively, with the third dimension varying over sub-wavelength shifts and the fourth varying over four-bucket positions. The variable `scene` stores an ambient light image of the scene to serve as the guide image for the bilateral filter, and the variable `lam` denotes the synthetic wavelength. The function `bilateralFilter` executes bilateral filtering of its first argument with its second argument as the guide image with `spatialWindow` and `intensityWindow`.

In addition, we provide in Algorithms 1 and 2 pseudocode for acquisition and reconstruction respectively using the general $\{M, N\}$ -shift phase retrieval algorithm.

Algorithm 1: Acquiring intensity measurements with swept-angle synthetic wavelength interferometry. The steps are captioned with reference to Figure 6 of the main paper.

Data: synthetic wavelength λ_s ; optical wavelength λ_o ; start position l

Result: intensity images $\mathcal{I}(x, l_n^m)$ at reference position l_n^m (defined below)

$l_n^m = l + n\lambda_s/N + m\lambda_o/M$ for $n \in \{0, \dots, N-1\}$ and $m \in \{0, \dots, M-1\}$;
 /* Capture the intensity images in Figure 6(a) */

for bucket positions $n \in \{0, \dots, N-1\}$ **do**
 for sub-wavelength shifts $m \in \{0, \dots, M-1\}$ **do**
 move reference mirror to position l_n^m ;
 capture image $I(x, l_n^m)$;
 end

end
return $I(x, l_n^m)$

Algorithm 2: Processing intensity measurements to estimate depth in swept-angle synthetic wavelength interferometry. The steps are captioned with reference to Figure 6 of the main paper.

Data: synthetic wavelength λ_s ; optical wavelength λ_o ; start position l ; bilateral filter hyperparameters: spatial kernel size σ_s and intensity kernel size σ_i ; intensity measurements $I(x, l_n^m)$ at reference position l_n^m (defined below); scene ambient-light image $S(x)$

Result: depth map $d(x)$
 /* Initialization */
 $l_{mn} = l + n\lambda_s/N + m\lambda_o/M$ for $n \in \{0, \dots, N\}$
 for $m \in \{0, \dots, M\}$;

for bucket positions $n \in \{0, \dots, M\}$ **do**
 /* Figure 6(b) */
 estimate interference-free image
 $\mathcal{I}(x, l_n) = \left(\sum_{m=0}^{M-1} I(x, l_n^m) \right) / M$;
 /* Figure 6(c) */
 estimate real parts of correlations
 $\text{Re} \{ \mathcal{C}(x, l_n^m) \} = I(x, l_n^m) - \mathcal{I}(x, l_n)$;
 estimate noisy envelope
 $\mathcal{E}^2(x, l_n) = \sum_{m=0}^{M-1} (\text{Re} \{ \mathcal{C}(x, l_n^m) \})^2 / 2M$;
 /* Figure 6(d) */
 denoise envelope using the bilateral filter
 $\mathcal{E}_{\text{bf}}^2(x, l_n) =$
 $\text{BilateralFilter}(\mathcal{E}^2(x, l_n), S(x), \sigma_s, \sigma_i)$;

end
 /* Figure 6(e) */
 estimate $d(x) = \frac{1}{2\kappa\epsilon} \arctan \left[\frac{\mathcal{E}_{\text{bf}}^2(x, l_3) - \mathcal{E}_{\text{bf}}^2(x, l_1)}{\mathcal{E}_{\text{bf}}^2(x, l_0) - \mathcal{E}_{\text{bf}}^2(x, l_2)} \right] + l$;
return $d(x)$

[5] Orazio Svelto. *Principles of Lasers*. 2010. 1, 2

References

- [1] Ioannis Gkioulekas, Anat Levin, Frédo Durand, and Todd Zickler. Micron-scale light transport decomposition using interferometry. *ACM TOG*, 2015. 4, 6
- [2] Alankar Kotwal, Anat Levin, and Ioannis Gkioulekas. Interferometric transmission probing with coded mutual intensity. *ACM TOG*, 2020. 4
- [3] Xiaomeng Liu, Kristofer Henderson, Joshua Rego, Suren Jayasuriya, and Sanjeev Koppal. Dense lissajous sampling and interpolation for dynamic light-transport. *Optics Express*, 2021. 4
- [4] Inc. Mirrorcle Technologies. Mirrorcle mems technical overview, 2022. https://www.mirrorcletech.com/pdf/Mirrorcle_MEMS_Mirrors_-_Technical_Overview.pdf. 2

```

1 function depth = reconstruct(frames, lam, spatialWindow, ...
2     intensityWindow, scene)
3 % Reconstruct depth from {4, 4}-shift swept-angle synthetic wavelength interferometry
4 % frames:           HxWx4x4 array of measurements, where the third dimension
5 %                   varies over subwavelength shifts and fourth over
6 %                   four-bucket positions
7 % lam:             synthetic wavelength
8 % spatialWindow:   spatial window for the bilateral filter
9 % intensityWindow: intensity window for the bilateral filter
10 % scene:           ambient light image of the scene
11
12 frames = im2double(frames)*4;
13 scene = im2double(scene)*4;
14
15 % Get interference-free images at each four-bucket position by averaging
16 % images captured with sub-wavelength shifts
17 interferenceFreeFrames = mean(frames, 3);
18
19 % Get interference images at each four-bucket position by subtracting
20 % interference-free images from the full images.
21 interference = frames - interferenceFreeFrames;
22
23 % Estimate the absolute values of the envelope by squaring and adding interference images
24 envelope = squeeze(sum(interference.^2, 3));
25
26 % Filter the estimated envelope with bilateral filtering using an ambient
27 % light image of the scene as the guide image
28 for position = 1:4
29     envelope(:, :, position) = bilateralFilter(envelope(:, :, position), ...
30                                             scene, spatialWindow, ...
31                                             intensityWindow);
32 end
33
34 % Apply the four-bucket phase retrieval algorithm to estimate phase
35 phase = atan2(envelope(:, :, 4) - envelope(:, :, 2), ...
36             envelope(:, :, 1) - envelope(:, :, 3));
37
38 % Convert phase to depth
39 depth = phase*lam/(2*pi);
40
41 end

```

Figure 8. Matlab code for recovering depth from {4, 4}-shift measurements